

Computational Investigation of the Operation of Heat Conservation Wheels in AHU-Systems

Eng. Asim M. Wafiah*

Prof. Ahmed Farouk Abdel Gawad

Prof. Muhammad N. Radhwi

College of Engineering & Islamic Architecture, Mechanical Engineering Department,
Umm Al-Qura University, Makkah Al-Mukarramah, Saudi Arabia, *Am907@hotmail.com

Computational Investigation of the Operation of Heat Conservation Wheels in AHU-Systems

Eng. Asim M. Wafiah
Prof. Ahmed Farouk Abdel Gawad
Prof. Muhammad N. Radhwi

ملخص

تعتبر "عجلات حفظ الطاقة" إحدى أهم الوسائل المستخدمة لاسترجاع الطاقة المفقودة من الهواء الراجع من غرف المرضى بالمستشفيات. وتتركز أهميتها في قدرتها على التبادل الحراري بين تيار الهواء الراجع من غرف المرضى (البارد نسبياً) وتيار الهواء الخارجي النقي الحار المسحوب لنظام التبريد من دون اتصال مباشر بين التيارين. حيث ينطوي هذا الاتصال المباشر على مخاطر صحية وبيئية جسيمة لما يمكن أن يسببه من انتشار الفيروسات والأمراض. وتتكون "عجلة حفظ الطاقة" من حلقة معدنية دائرية لها خاصية نفوذية تسمح بمرور الهواء وتعمل بين تيارَي الهواء الراجع من غرف المرضى والهواء الجوي النقي الداخل. ويتم تحريك العجلة بمحرك كهربائي بسرعة منخفضة نسبياً بحيث يتم تمرير الهواء الراجع والهواء النقي بالتناوب بين أجزاء العجلة. ويركز هذا أيضاً البحث على دراسة أداء "عجلات حفظ الطاقة" والتي تعتبر المكون الرئيسي في منظومة التبريد في كثير من المستشفيات. حيث تم تطوير نموذج حسابي وتطبيقه لتحديد تأثير العوامل المختلفة على أداء العجلة. وقد تم تسجيل العديد من الملاحظات القيمة والاستنتاجات المهمة بناءً على هذه الدراسة.

Abstract

In certain facilities with concern to air-conditioning systems, a heat transfer process is to be applied to heat recovery of the disposing return-air from the patient's room without contamination. Therefore, much attention has been paid recently to the conservation wheels.

Conservation wheel consists of a rotor with permeable storage mass fitted in a casing, which operates intermittently between a hot and cold fluids. The rotor is driven by a motor with relatively low speed so that the exhaust air and fresh air are alternately passed through each section. In this work, concentration is paid to the conservation wheel, which is the main component of the wheel air-conditioning system along with a parametric study to investigate the influence of the different parameters. A computational model will be developed and validated by comparison to the results of others. The computations are to be carried out using the commercial package ANSYS – FLUENT, validation of the present computational model and technique was carried out successfully. Thus, present results can be taken with big confidence.

1. Introduction

There is a growing demand for energy saving technologies in buildings due to global warming, environmental impact issue and the rapid consumption of oil resources. As a result to this, energy-efficient technologies are becoming more popular amongst researchers and designers. In this regard, to fulfill energy conservation demands, researchers have focused on the development of advance heat or energy recovery with energy-efficient ventilation system.

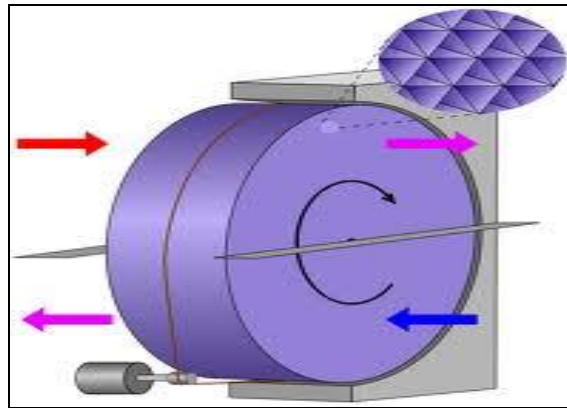


Fig. 1: Heat Conservation Wheels [1]

Heat-recovery wheel (Fig. 1) consists of a rotor with permeable storage mass fitted in a casing, which operates intermittently between a hot and cold fluid. The rotor is driven by a motor with relatively low speed so that the exhaust air and fresh air are alternately passed through each section.

1.1 Previous Investigation

Much effort is devoted in the research and application of heat conservation wheel components, especially desiccant wheels [1-9]. Also, there are studies concentrated on the potential use of heat conservation wheel systems in various locations in the USA and Europe [10-12].

1.2 Present Investigation

In this work, attention is paid to the rotary heat conservation wheel, which is the main component of the heat conservation wheel air-conditioning system. A computational model was developed and validated by comparison to the results of others. The computations were carried out using the commercial package ANSYS - FLUENT.

Nomenclature

Symbol	Description
A	Heat flow cross-area (m^2)
A_w	Cross-area of matrix (m^2)
B_w	Length of the surface through which heat transfer (m)
C_p	Specific heat at constant pressure ($J/(kg \text{ } ^\circ C)$)
C	Thermal capacity rate of flow stream one side ($J/(s \text{ } ^\circ C)$)
Cr	Ratio of heat capacity of the matrix to the minimum air heat capacity rate in a rotary air-to-air heat exchanger, thermal capacitance
D	Inner diameter of the circular tube on one side estimated by all the free-flow flute (m)
D	Diameter of flute (m)
G_k	Production of turbulence kinetic energy
H	Convective heat transfer coefficient of fluid flow ($W/(m^2 \text{ } ^\circ C)$)
K	Thermal conductivity ($W/(m \text{ } ^\circ C)$)
k_{eff}	The effective thermal conductivity
k_t	Turbulent thermal conductivity
L	Length of heat wheel (m)
λ	Coefficient of bulk viscosity
\dot{m}	Mass flow rate (kg/s)
M	Mass (kg)
Nu	Nusselt number
Pr	Prandtl number
Q	Heat transfer rate on whole cross-area (w)
q''	Heat flux, heat transfer rate per unit of surface area (w / m^2)
$Ratio$	Ratio of minimum to maximum air heat capacity rates in an air-to-air heat Exchanger
R	Heat transfer resistance ($m^2 \text{ } ^\circ C/W$)
Re	Reynolds number
S_h	Volumetric heat source
S	Modulus of the mean rate-of-strain tensor
T	Temperature (K)
U	Total heat transfer coefficient ($W/(m^2 \text{ } ^\circ C)$)

$\overline{u^2}$	Normal stress
V	Velocity of airflow (m/s)
Greek Letters	
ϵ_{cf}	Effectiveness of counter flow heat exchanger
μ	Absolute viscosity coefficient (kg/(m s))
ϕ	Rotational frequency (revolution per second)
ρ	Density (kg/m ³)
$(\tau)_{eff}$	The deviatoric stress tensor
ν	Kinematic viscosity coefficient (m ² /s)
Superscripts & Subscripts	
C	Cold fluid side of heat exchanger
E	The total energy
F	Fluid
H	Hot fluid side of heat exchanger
Hy	Hydraulic
In	Inlet
Max	Mmaximum value
min	Minimum value
out	Outlet
W	Wheel matrix
Abbreviations	
AHU	Air handling unit
$ASHRAE$	American Society of Heating, Refrigerating and Air Conditioning Engineers
CFC	Chlorofluorocarbons
$HVAC$	Heating, ventilation and air conditioning
NTU	Number of transfer unit

2. Literature Review

Different methods of numerical solution have been used by many researchers with different simplified treatments of the fluid and solid domains to predict the behavior of air systems. The modeling of the performance of desiccant wheels is of great relevance for product optimization by the manufacturer as well as to perform parametric studies and yearly simulations of the performance of global systems integrating heat conservation wheel, towards a more rational energy use. From this viewpoint, much attention has been paid recently to a heat conservation wheel air-

conditioning system as an alternative to the conventional mechanical dehumidification system.

The optimum temperature and humidity range for human comfort is presented by ASHRAE [3]. In addition, the forced ventilation has become necessary because the air tightness of buildings has been increasing. Zhang and Niu [14] indicated that a chilled-ceiling combined with desiccant cooling could save up to 40% of primary energy consumption when compared to a conventional constant air volume system.

Ge et al. [15] reviewed the literatures on mathematical models for the rotary desiccant wheel and classified the models according to the modeling types of the heat and mass transfer between the humid air in air channel and the wheel wall.

For example, Holmberg [16] developed the mathematical model using the overall heat and mass transfer coefficients to express the heat and mass transfer between the humid air in air channel and the wheel wall. The adsorption isotherm in this study is assumed to be a linear function. San and Hsiau [17] considered the heat and mass transfer in air channel side and wheel wall-side separately and developed the mathematical model. In the air channel side, the model is unidimensional, based on convective heat and mass transfer.

In the heat conservation wheel wall-side, the model is one-dimensional too and based on the mass diffusion and heat conduction. Only surface diffusion is considered inside the desiccant wall. They investigated the effect of several parameters, for example the number of transfer units, on the performance of the desiccant wheel using the mathematical model that they developed.

Charoensupaya and Worek [18] developed the mathematical model considering both side heat and mass transfer separately. In the air channel side, the convective heat and mass transfer coefficients are assumed to be constant. In the wheel wall side, both the pore diffusion and surface diffusion were considered. Their model is validated by comparison with experimental data of isothermal adsorption. They analyzed the effect of several important parameters, especially heat and mass transfer Biot numbers, on the performance of the desiccant cooling system

3. System Description

3.1 Chilled-Water Air-Conditional System

In a chilled water air conditioning system (Fig. 2), cold water is flowing through the coil that cools the room's air. In the chiller, refrigerant flows through the coil that cools the chilled water. The chilled water is pumped through a piping loop to air handlers in the spaces to be cooled, where it absorbs heat from the air that flows over the air handling coil. The warmed up water then returns through the piping loop back to the chiller, where the heat absorbed is released to the refrigerant flowing through the chiller's evaporator coil.

The chilled water circuit of a typical water chiller system consists of a pump, cooling coils, expansion tank, and piping valves and controls, in a closed loop.

Normally, a heatrecovery system in buildings consists of: (i) Duct for incoming fresh air and return contaminated air. (ii) Heat exchanger core, where heat is transferred from one stream to the other. (iii) Two blower fans; the first fan is to supply fresh air, the other fan is to drive return air.

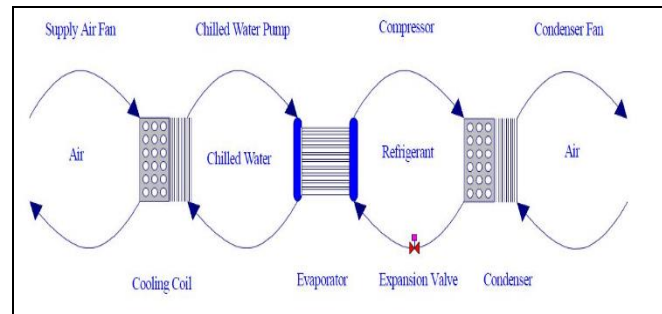


Fig. 2: Chilled water system [5]

3.2 Heat Conservation Wheel

Heat conservation wheel consists of a rotor with permeable storage mass fitted in a casing which operates intermittently between hot and cold fluid. The rotor is driven by a motor so that the exhaust air and fresh air are alternately passed through each section. Rotor speed is normally relatively low and in a range of 3-15 rpm [15]. A unique advantage of rotary wheels is the capability of recovering both sensible and latent heat.

Heat conservation wheels are widely used and the units are known for their high efficiency and trouble-free operation. Temperature efficiencies above 80% are not uncommon. Research on this field keeps active in recent years and involve many theoretical and experimental aspects of heat conservation wheel for building applications [22]. One of the earliest investigations of heat conservation wheel was performed by Sauer and Howell [23]. For clinical application in hospitals, it uses a technology to coat Ion Exchange Resins (Desiccant) on the aluminum sheet in a rotor. This substrate is further coated with a layer of Anti-Bacteria and Anti-Mold agent which prevents propagation and survival of bacteria and mold.

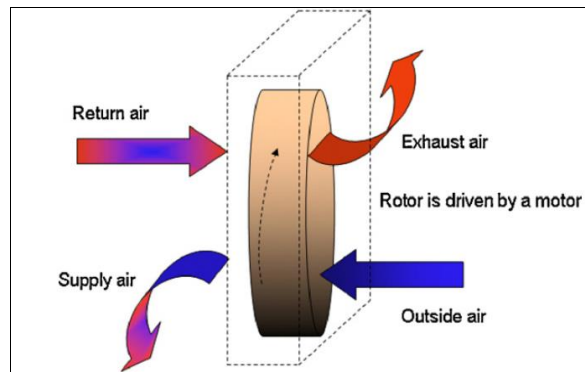


Fig. 3: Heat conservation wheel

As seen in (Fig. 3) return air from the inside passes from the upper half of the cassette through the rotor and is exhausted outside. During this, most of the total heat (heat and moisture) of the return air is kept in the rotor and soiled air only is exhausted. On the other hand, when outdoor air, taken in from the lower half of the cassette, passes through the rotor, the outdoor air receives total heat that the rotor has kept and is pre-heated in winter and pre-cooled in summer to be thus supplied continuously to the inside. In other words, the total heat exchanger is an energy saving equipment that recycles energy lost in ventilation.

3.3 Shapes of the Heat Recovery Wheel

(Fig. 4) shows different shapes of the desiccant wheels and the close-up of the front surface. They may have different values of width (20, 60, 100, 200, 400 mm) with diameter (350 mm).

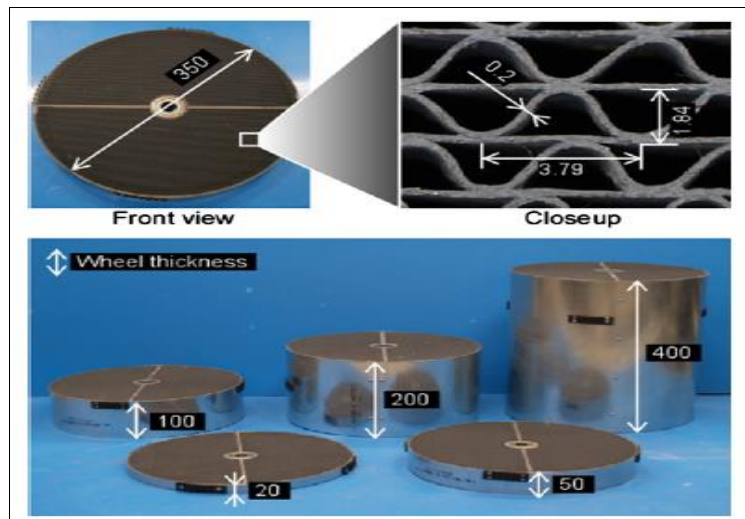


Fig. 4: Different shapes of Heat Recovery wheels. [2]

3.4 Present Work

In this work, a numerical model is used to study and discuss the performance of a desiccant cooling system in terms of its heat transfer efficiency. The

commercial codes ANSYS and Fluent 13 were utilized to carry out the investigation. The investigated components of the heat conservation wheel have the cross-sectional shape of a circle, hexagonal and sinusoidal with four different materials: (steel, aluminum, nickel and copper) and three velocities.

4. Mathematical Model & Numerical Treatment

4.1 Development of Mathematical Model

For numerical analysis it is assumed that the flow is incompressible, unidimensional. Thermal properties of the fluid (such as specific heat, thermal conductivity, density) are assumed to have bulk average values and be uniformed at any cross-section. Mass flow rate is constant. Heat transfer is axial to the flow direction. Based on the assumptions discussed before, differential equations relating the fluid and matrix temperatures can be derived from the energy balance equation applied to a unit element dz through the heat wheel for a control volume. In what follows, we denote by T the temperature of fluid and the matrix which is a function of time t and distance z , $T=T(t, z)$.

Furthermore, in all discussions related to the fluid airflow we use subscript 'f' with $f = (f_h, f_c)$ to indicate the air extracted from the room to the exhausted duct (denoted by f_h) or the air supplied from outdoor to the room (denoted by f_c). Finally, we use subscript 'w' in our discussion of the wheel matrix.

Our starting point is the energy balance equation given in the following form:

$$\dot{Q}_{in} + \dot{W} + q_{w-f}'' = \dot{Q}_{out} + \left(\frac{dE}{dt}\right)_{CV} \quad (4.1)$$

where $\dot{Q}_{in} = \dot{W} + q_{w-f}''$ is the energy-input rate with $\dot{Q}_{in} = [\dot{m} \cdot (e + Pv)]_{in} = [\dot{m} \cdot (KE + PE + u + Pv)]_{in}$, e the total energy of the matter (fluid or gas) per unit mass, u the internal energy, KE the bulk kinetic energy, PE the bulk potential energy, Pv the flow work, that is, the amount of energy transfer as work (associated with a unit of mass), \dot{W} the sum of shaft-power input and power input due to normal motion of the control-volume boundaries, q_{w-f}'' the sum of all heat transfer rates from the wheel matrix to the fluid for the control volume, $\dot{Q}_{out} = [\dot{m} \cdot (e + Pv)]_{out}$ the energy-output rate and $\dot{E} = \left(\frac{dE}{dt}\right)_{CV}$ is the energy-storage rate.

The analysis is based on Eq. (4.1) considered in the uni-dimensional approximation. Heat convection and heat conduction are analyzed here in the fluid direction over the control volume of (a) each fluid airflow within cross-areas A_{f-h} and A_{f-c} and (b) the wheel matrix within cross-area A_w . Note that A_{f-h} and A_{f-c} are the sum of the areas of each channel on the fluid sides, while A_w is the effective area of the thin plate from the simplified wheel matrix.

In (Fig. 5), we present the diagram for model simplification and provide all necessary details of our definition of the control volume element definition.

Eq. (4.1) for control volume elements of the extracted air was used, r , the wheel matrix and the supply air. Fig. 5 illustrates the present approach in greater details.

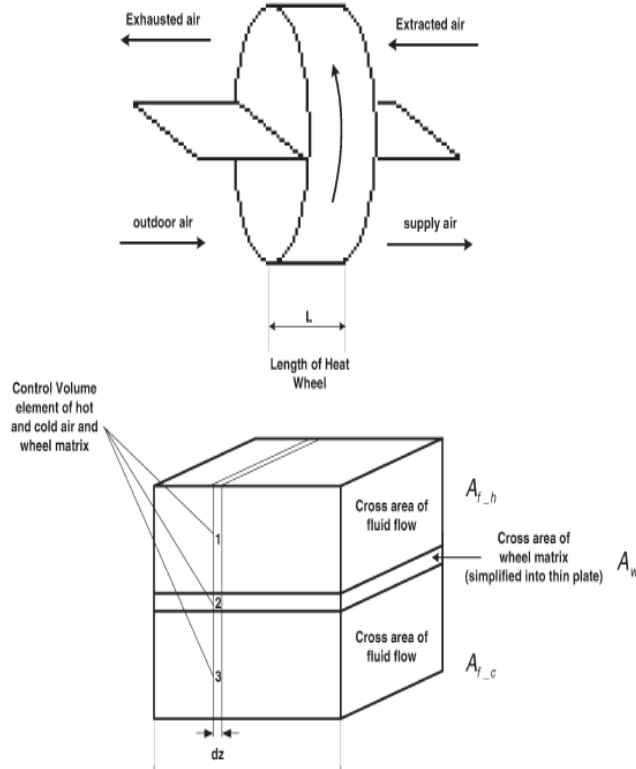


Fig. 5: Diagram of thermal model simplification and control volume element definition. [13]

In particular, for the control volume elements presented in (Fig. 6) we have the following relationships (written for the extracted air, the wheel matrix and the supply air, respectively):

$$\begin{aligned} \dot{Q}_{f-h,z+dz} - (\lambda_{f-h} \cdot A_{f-h} \frac{\partial T_{f-h}}{\partial z} |_{z+dz}) - \\ \lambda_{f-h} \cdot A_{f-h} \frac{\partial T_{f-h}}{\partial z} |_z = \dot{Q}_{f-h,z} + q_{f-h-w}'' + \\ \frac{dE_{f-h}}{dt}, \end{aligned} \quad (4.2)$$

$$\begin{aligned} \frac{dE_w}{dt} = q_{f-h-w}'' + q_{w-f_c}'' + \\ \left(\lambda_w \cdot A_w \frac{\partial T_w}{\partial z} |_{z+dz} - \lambda_w \cdot A_w \frac{\partial T_w}{\partial z} |_z \right) \end{aligned} \quad (4.3)$$

$$\dot{Q}_{f-c,z} + q_{w-f_c}'' + (\lambda_{f-h_c} \cdot A_{f-h_c} \frac{\partial T_{f_c}}{\partial z} |_{z+dz}) -$$

$$\lambda_{f_c} \cdot A_{f_h} \frac{\partial T_{f-c}}{\partial z} \Big|_z = \dot{Q}_{f_c, z+dz} + \frac{dE_{f-c}}{dt} \quad (4.4)$$

In (4.2)–(4.4), for both \dot{Q}_{f-h} and \dot{Q}_{f-c} we have:

$$\dot{Q} = \dot{m}h = \dot{m}c_p \Delta T \quad (4.5)$$

Furthermore, we have $KE = 0$, $PE = 0$ in \dot{Q} and $u + Pv = h$,

$$\frac{dE}{dt} = \dot{M}h = \dot{M}c_p \frac{dT}{dt} \quad (4.6)$$

$$q'' = U \cdot B_w (T_w - T_f) dz \quad (4.7)$$

For both E_{f-h} , E_{f-c} , E_w and q''_{f-h-w} , q''_{w-f-c}

$$\lambda A \frac{\partial T}{\partial z} \Big|_{z+dz} - \lambda A \frac{\partial T}{\partial z} \Big|_z = [\lambda A \frac{\partial T}{\partial z}]_{z+dz} = \lambda A \int_z^{z+dz} \frac{d}{dz} \left(\frac{dT}{dz} \right) d\xi \quad (4.8)$$

By substituting Eqs. (4.5)–(4.8) into Eqs. (4.2)–(4.4), we obtain a set of three equations:

- For the extracted air:

$$\begin{aligned} \dot{m}_{f-h} h_{f-h, z+dz} - \lambda_{f-h} \cdot A_{f-h} \int_z^{z+dz} \frac{\partial}{\partial z} \left(\frac{\partial T_{f-h}}{\partial z} \right) d\xi \\ = \dot{m}_{f-h} h_{f-h, z+dz} + \int_z^{z+dz} B_w U (T_{f-h} - T_w) d\xi + \frac{\partial}{\partial t} \int_z^{z+dz} (A_{f-h} \rho_{f-h} h_{f-h}) d\xi \end{aligned} \quad (4.9)$$

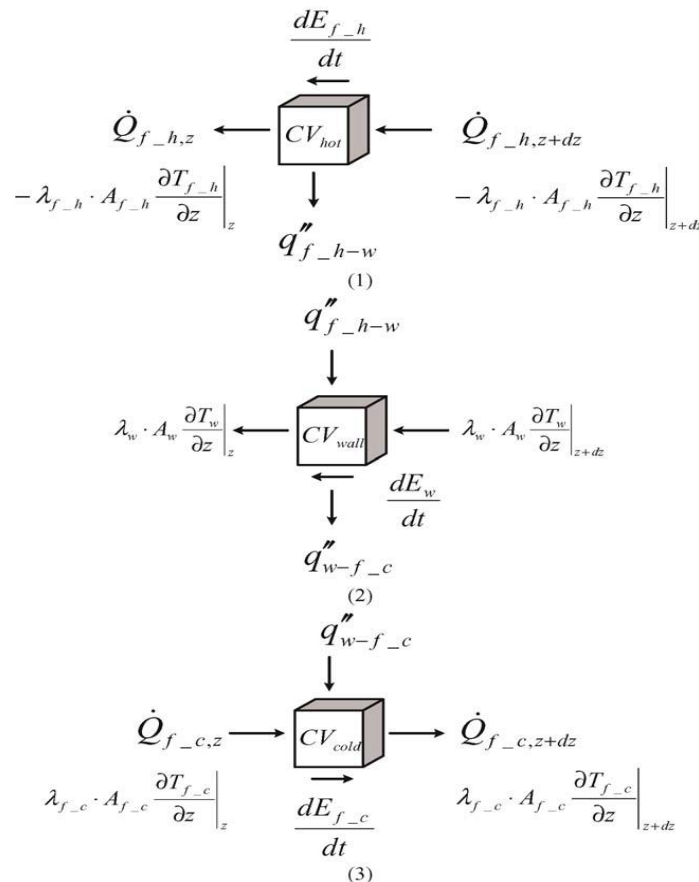


Fig. 6: Schematic diagram describing the energy balance analysis for a control volume of: (1) extracted air; (2) wheel matrix; (3) supply air. [13]

- For the supply air:

$$\begin{aligned} \dot{m}_{f_h} h_{f_c,z} + \int_z^{z+dz} B_w U (T_w - T_{f_c}) d\xi + \lambda_{f_c} \cdot A_{f_c} \int_z^{z+dz} \frac{\partial}{\partial z} \left(\frac{\partial T_{f_c}}{\partial z} \right) d\xi \\ = \dot{m}_{f_c} h_{f_c,z+dz} - \frac{\partial}{\partial t} \int_z^{z+dz} (A_{f_c} \rho_{f_c} h_{f_c}) d\xi \end{aligned} \quad (4.10)$$

- For the wheel matrix:

$$M_w C_{p,w} \frac{\partial T_w}{\partial t} = UB_w L (T_{f_h} - T_w) - UB_w L (T_w - T_{f_h}) + \lambda_w \cdot A_w \cdot L \left(\frac{\partial^2 T_w}{\partial z^2} \right) \quad (4.11)$$

In the context of (4.9)–(4.11) we note that

$$\begin{aligned} \dot{m}_{f_h} h_{f_h,z+dz} - \dot{m}_{f_h} h_{f_h,z} = [\dot{m}_{f_h} h_{f_h,z+dz}]_z^{z+dz} = \\ = \dot{m}_{f_h} \int_z^{z+dz} \frac{\partial h_{f_h}}{\partial z} d\xi, \end{aligned} \quad (4.12)$$

$$\dot{m}_{f_c} h_{f_c,z+dz} - \dot{m}_{f_c} h_{f_c,z} = [\dot{m}_{f_c} h_{f_c,z+dz}]_z^{z+dz} = \dot{m}_{f_c} \int_z^{z+dz} \frac{\partial h_{f_c}}{\partial z} d\xi, \quad (4.13)$$

$$h = C_p (T - T_{ref}) \quad (4.14)$$

4.2 Turbulence Modeling

4.2.1 Realizable k - ε turbulence model

The realizable k - ε turbulence model was used in the present study. The realizable k - ε model differs from the standard k - ε model in two important ways:

- The realizable k - ε model contains an alternative formulation for the turbulent viscosity.
- A modified transport equation for the dissipation rate, ε , has been derived from an exact equation for the transport of the mean-square vorticity fluctuation.

For further details about the realizable k - ε turbulence model, one may refer to [22].

5. Computational Aspects

In this section the computational aspects of the solution of the governing equations that were presented in section (4) are explained. Moreover, the examined test case are also shown. The results of these test cases will be presented and discussed in the next section. As mentioned in Sec.3, the conservation wheel contains flow passages that form a matrix of similar channels. The present study concerns the flow and thermal fields through these channels. As these channels are similar, only one complete channel is considered.

The flow was treated as steady without the effect of wheel rotation. The flow in the channel was kept hotter than the surroundings. Due to the nature of the AHU

system, the channel flow is treated as turbulent. The realized k- ϵ model (Sec.4) was adapted to solve the turbulent flow.

5.1 Computational Domain and Boundary Conditions

The computational domain, for all test cases, is a three dimensional (3-D) domain, Fig.7. The ratio between the length of the channel and its hydraulic diameter (L/D) is (100/3).

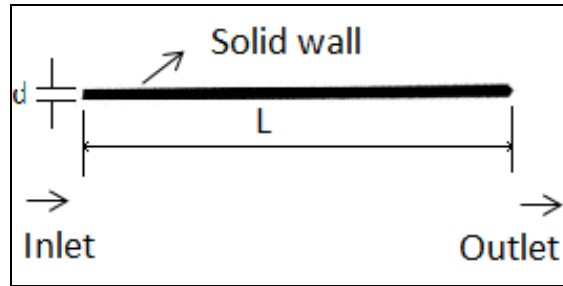


Fig.7: Computational domain and boundary Condition

Typically, these are three types of boundary conditions that can be listed as:

- **Inlet boundary condition:** inlet uniform velocity is specified at the entrance of the channel. According to ASHRAE handbook (2005), the inlet temperature was taken as 319K. This temperature value represents the annual average ambient temperature in Makkah.
- **Outlet boundary condition:** Pressure outlet and temperature 300 K
- **Wall boundary condition:** the walls of the channel were treated as smooth. The no-penetration and no-sliding conditions were applied at the channel walls. The temperature at the inner surface of the walls was kept at 309 K for all test cases. This makes a temperature difference of 10K between the inlet flow and the inner surface. This difference value was recommended in the literature [13]. The wall material changes depending on the test case (Sec.5.3).

5.2 Computational Grid (Mesh)

Due to the complexity of the geometry of the channels, the computational domain was discretized using unstructured grids. This type of grids usually grants the flexibility to generate enough computational points in locations of severe gradients. Unstructured grids adopt themselves easily to irregular geometries with minimum programmer's effort.

The computational domain was covered by tetrahedral-shaped elements, (Fig. 8). The grid is very fine next to the solid boundary. The dimensionless distance between the wall and first computational point $y^+ \approx 2$. y^+ is calculated as

$$y^+ = \frac{u_\tau y}{\nu} \quad (5.1)$$

Where, y is the distance to the first point off the wall, ν is the kinematic viscosity, u_τ is the friction velocity.

$u_\tau = \sqrt{\frac{\tau}{\rho}}$, τ is the wall shear stress and ρ is the flow density. The value of $y^+ = 2$ ensures the resolution of the complex turbulent flow.

5.3 Grid Size and Independency

Careful consideration was paid to ensure the grid-independency of the computational solution.

Thus, three grid sizes were used to test the grid-independency, namely: 100,000, 150,000 and 200,000 elements (cells).

The results of both the flow and thermal fields show that the difference between the results of the second and third grid is within in the range of 1-2 %.

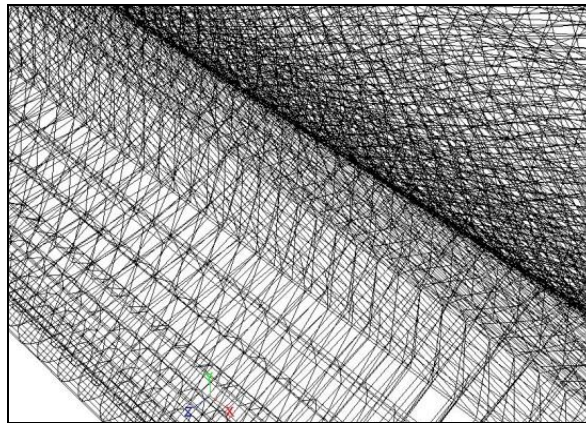


Fig.8: Enlarged grid structure (sample)

Thus, the second grid size (150,000) was used for all the test cases.

5.4 Numerical Method

Simple algorithm (Semi-implicit method for pressure – linked equations) was employed to solve for the velocity and pressure fields. Each equation of the momentum and energy was solved by "first-order upwind" scheme. The "standard wall function" was used as the near-wall treatment technique in the turbulence model. The solution continues until the numerical residual (error) of all quantities get below 10^{-5} .

5.5 Test cases

A parametric study was carried out to obtain the best case for optimum operation. Different cases were computationally tested and evaluated. The

parametric study covered the shape of the channel cross-section, the wall material, and the flow Reynolds number.

Three cross-sectional shapes were considered, circular, hexagonal and sinusoidal. The sinusoidal cross-section is widely used in conservation wheels. It is used here mainly for comparison. The other two shapes are proposed by the author. The hexagonal shape has good characteristics when considering flow and thermal fields. On the other hand, the Lozenge shape has good structural properties.

Four materials were tested as walls of the channels, namely: copper, aluminum, nickel and steel.

The calculation were performed at three values of Reynolds numbers 1540, 1950 and 2300. Reynolds number is calculated based on inlet velocity and the hydraulic diameter of the channel, i.e.,

$$Re = \frac{u_{in} d_h}{\nu}$$

Where, u_{in} is the inlet velocity (4 m/s), d_h is the hydraulic diameter (3 mm), ν is the kinematic viscosity

$$d_h = \frac{(4) \cdot Area}{Perimeter}$$

This combination of parameters leads to thirty six (36) test cases. Table.1 shows a summary of all the studied test cases.

5.6 Validation of the Numerical predicted data

In the present work, the present numerical results compare very well to the experimental data obtained by others [13] as shown in Fig.9 for the temperature contours

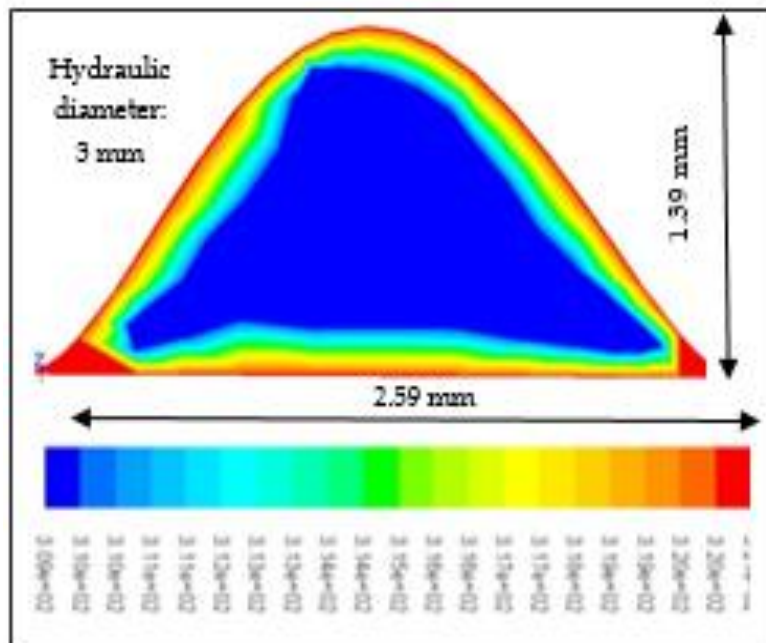


Fig.9: Temperature field, cross-sectional view, Present computational predictions.

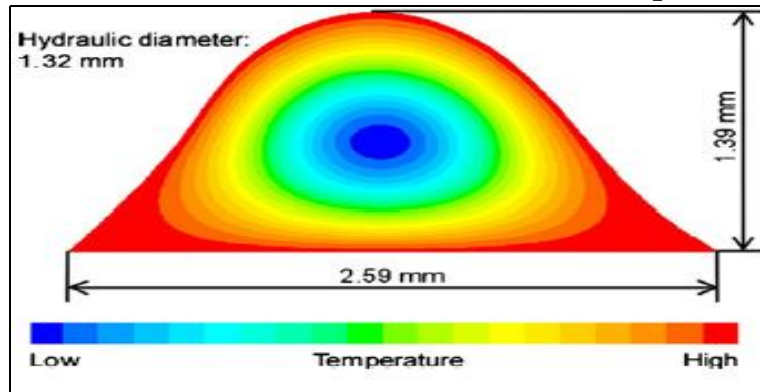



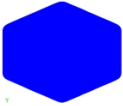

Fig.10: Temperature field, cross-sectional view, Experimental work [13]

Generally, the same trend of temperature distribution and gradient is obtained in both Fig. 9 and Fig. 10. The red color means high temperature and blue color means low temperature. More gradient contours appear in Fig. 10. This may be attributed to the secondary flow that is not considered in the present computational investigation.

6. Results and Discussions

This section demonstrates the results of the computations of the test cases that were mentioned in section 5 and table 1.

Table. 1: Summary of the test case

Shape	Material	Reynolds No.
Circle 	Copper	1540
	Aluminum	1950
	Nickel	
	Steel	2300
Hexagonal 	Copper	1540
	Aluminum	1950
	Nickel	
	Steel	2300
Sinusoidal 	Copper	1540
	Aluminum	1950
	Nickel	
	Steel	2300

The carried-out parametric study aims to find the combination of parameters that gives the optimum performance of the wheel. Optimum performance, here, means best heat transfer exchange rate.

However, the results must cover both the flow and thermal fields. The flow field concerns the working fluid (air) that transfers heat. Thus, the flow field of the different cases is presented firstly. Then, the thermal fields results are presented. Naturally, concentration is paid to the thermal field as heat transfer optimization is the principal goal of the study.

6.1 Flow Field

6.1.1 Circle cross-section

Fig. 11. Shows the velocity contours at the entrance and exit of the channel at $Re = 1950$ and aluminum. It is clear from the velocity contours at exit that the flow becomes fully developed before the channel exit.

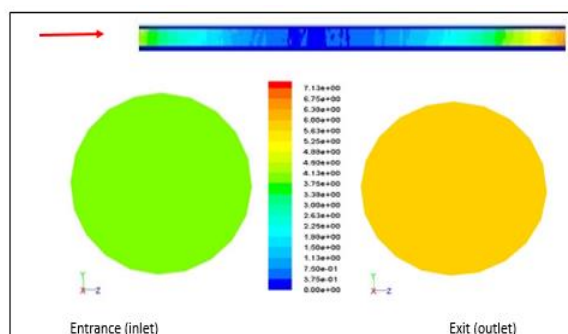


Fig. 11. Velocity contours for $Re= 1950$, Aluminum

The same pattern of Fig.11 is repeated typically for all test cases. This ensures the fully developed nature of the flow inside the channel. However, the entrance length may change from one case to another. This variation of entrance length affects the thermal field greatly as will be explained in the coming sections.

Fig. 12 shows the pressure distribution along the channel as well as at entrance and exit for $Re= 1950$ and aluminum material,

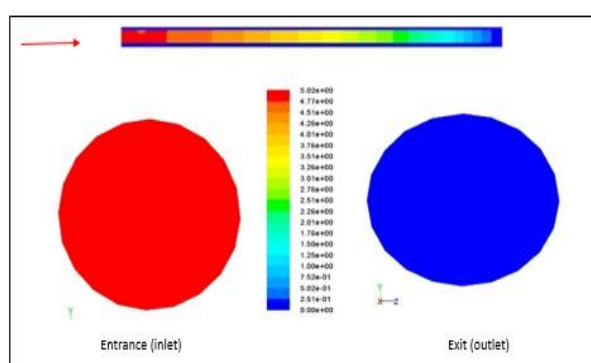


Fig. 12. Pressures Contours

It is clear from Fig. 12 that the flow in the channel causes a considerable pressure drop from the entrance to the exit. The same pattern of Fig. 12 is obtained for all test cases.

6.1.2 Hexagonal cross-section

Fig. 13. Shows the velocity contours at the entrance and exit of the channel at $Re = 1950$ and aluminum. It is clear from the velocity contours at exit that the flow becomes fully developed well- before the channel exit.

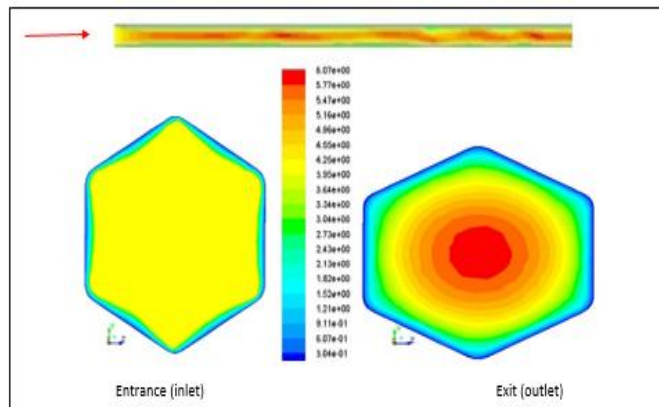


Fig. 13. Velocity contours for $Re= 1950$, Aluminum

The same pattern of Fig.13 is repeated typically for all test cases. This ensures the fully developed nature of the flow inside the channel. However, the entrance length may vary from one case to another. This variation of entrance length affects the thermal field greatly as will be explained in the coming sections.

Fig. 14 shows the pressure distribution along the channel as well as at entrance and exit for $Re= 1950$ and aluminum material.

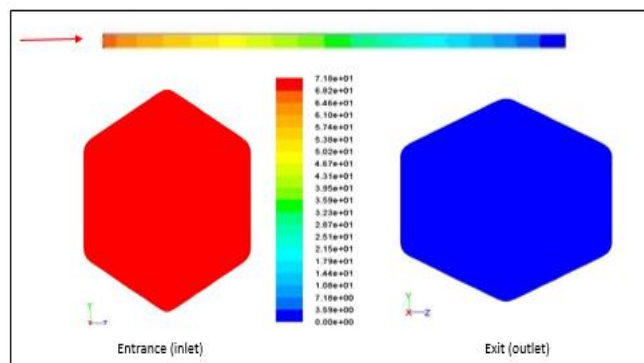


Fig. 14. Pressures Contours

It is clear from Fig. 14 that the flow in the channel causes a considerable pressure drop from the entrance to the exit. The same pattern of Fig. 14 is obtained for all test cases.

6.1.3 Sinusoidal cross-section

Fig. 15. Shows the velocity contours at the entrance and exit of the channel at $Re= 1950$ and aluminum. It is clear from the velocity contours at exit that the flow becomes fully developed well-before the channel exit.

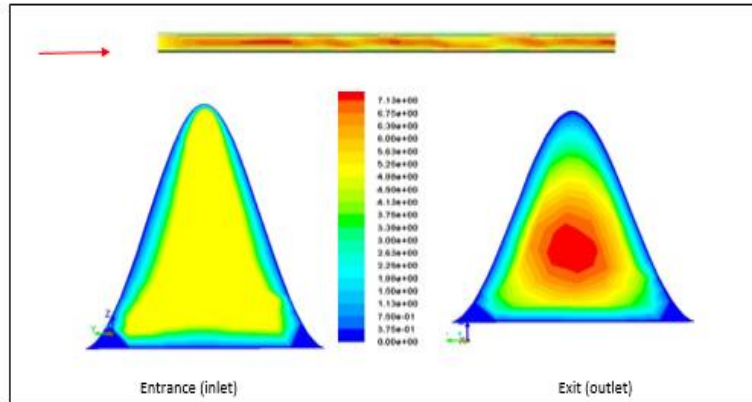


Fig. 15. Velocity contours for $Re= 1950$, Aluminum

The same pattern of Fig.15 is repeated typically for all test cases. This ensures the fully developed nature of the flow inside the channel. However, the entrance length may vary from one case to another. This variation of entrance length affects the thermal field greatly as will be explained in the coming sections.

Fig. 16 shows the pressure distribution along the channel as well as at entrance and exit for $Re= 1950$ and aluminum material,

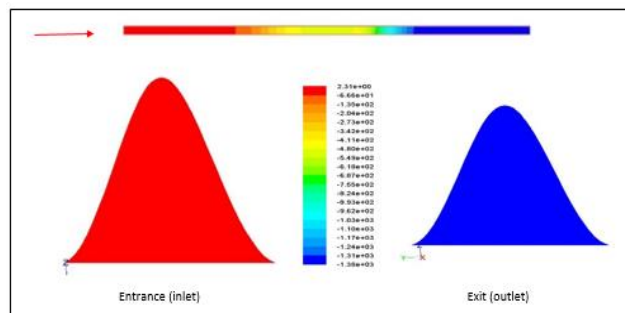


Fig. 16. Pressures Contours

It is clear from Fig. 16 that the flow in the channel causes a considerable pressure drop from the entrance to the exit. The same pattern of Fig. 16 is obtained for all test cases.

6.2 Thermal Field

To estimate the effect of different parameters on the heat transfer along the channel a certain criterion should be established. This criterion concerns the different thermal zones along the channel in the stream-wise direction.

The length of the channel was divided into three consequence zones; hot, middle and cold. For generality the lengths of the three zones are normalized by the total length of the channel. Thus, these lengths can be defined as, Fig. 17:

1. Hot zone percentage relative length

$$L_h = \frac{\text{Length of hot zone}}{\text{Channel total length}} \times 100$$

2. Middle (Transitional) zone percentage relative length

$$L_m = \frac{\text{Length of middle zone}}{\text{Channel total length}} \times 100$$

3. Cold zone percentage relative length

$$L_c = \frac{\text{Length of cold zone}}{\text{Channel total length}} \times 100$$

Apparently, the greater the value of L_c , the better the heat transfer process is.

This criterion was implement in the present study to determine the combination of parameters that gives the optimum heat transfer process.

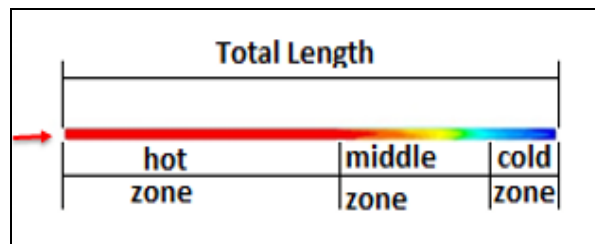


Fig.17. Thermal zones along the channel length

6.2.1 Circle cross-section

Fig. 18 shows the temperature contours along the channel as well as at entrance and exit section for $Re= 1950$ and aluminum material.

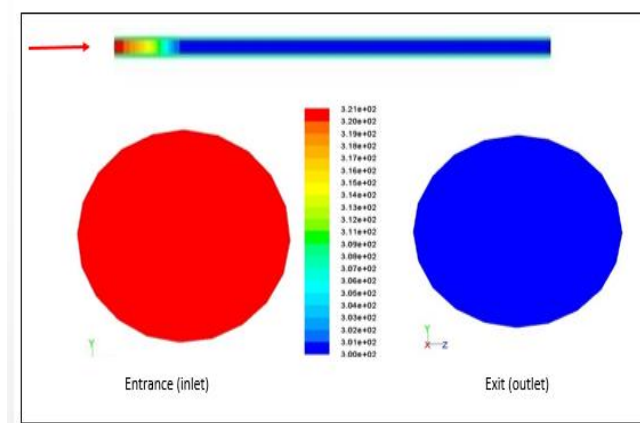


Fig. 18. Temperature Contours $Re= 1950$, Aluminum material

It is clear from Fig.18 that the temperature inside the channel drops from the inlet temperature to the wall temperature well before exiting the channel. The pattern of temperature contours at entrance and exit of the channel is repeated for all cases. However, the temperature contours along the channel length changes from one case to another depending on the case parameter.

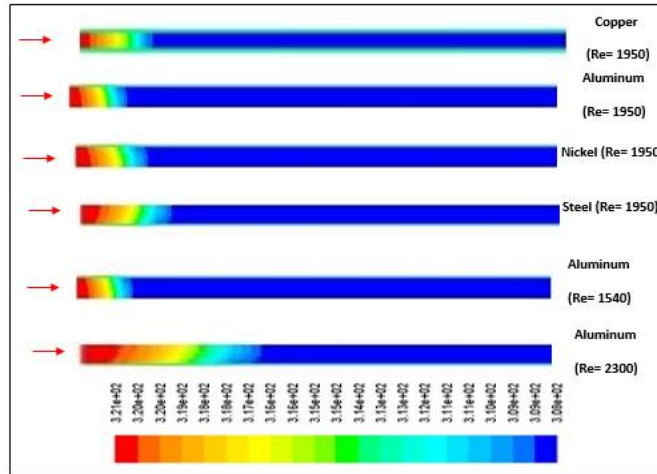


Fig. 19. Temperature Contours for all Materials of Circle cross-section

Fig.19 shows the temperature contours along the channel length for all cases. Based on the results of Fig. 19, the percentage relative lengths of the thermal zones along the channel for different cases are shown in Fig. 20

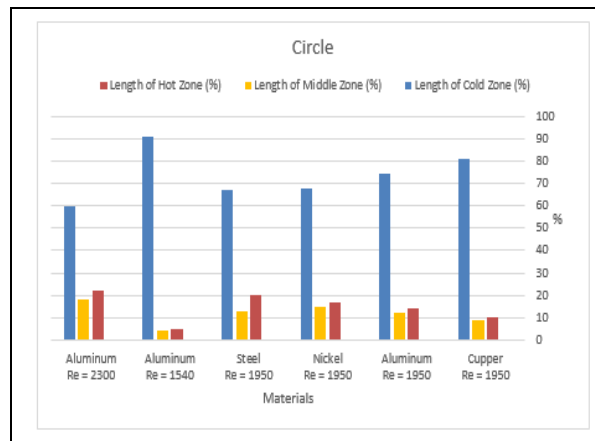


Fig. 20. Bar chart for the Circle shape identifying the three zones

It is clear from Fig.20 that the cold zone has the longest percentage relative length. It is clear from Fig.20 that at the same Reynolds number of 1950, the longest cold zone has a percentage relative lengths of $L_c = 81\%$ and $L_h = 10\%$ for the copper material. When considering aluminum as the wall material at different values

of Reynolds number, the longest cold zone has a percentage relative lengths of $L_c = 91\%$ and $L_h = 5\%$ at $Re = 1540$

6.2.2 Hexagonal cross-section

Fig. 21 shows that temperature contours along the channel as well as at entrance and exit section for $Re = 1950$ and aluminum material.

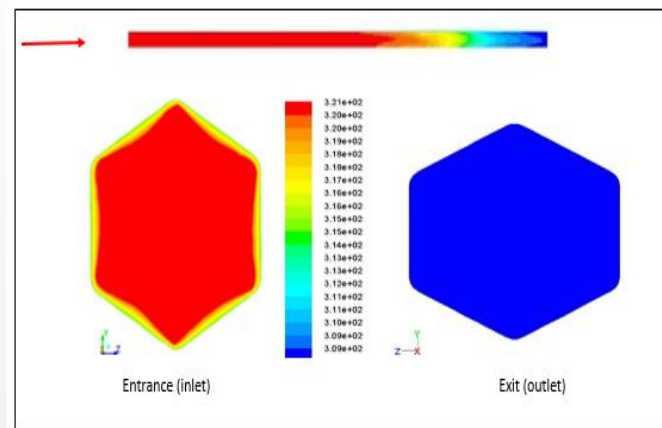


Fig. 21. Temperature Contours $Re = 1950$, Aluminum material

Fig.21 shows that the temperature inside the channel drops from the inlet temperature to the wall temperature well before exiting the channel. The pattern of temperature contours at entrance and exit of the channel is repeated for all cases.

However, the temperature contours along the channel length changes from one case to another depending on the case parameter. Fig.22 shows the temperature contours along the channel length for all cases.

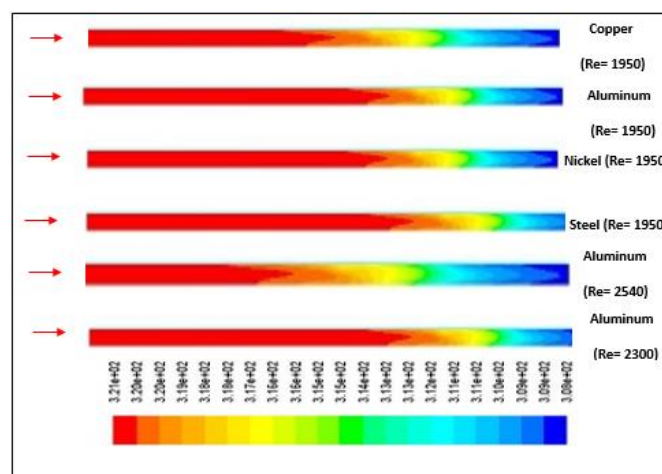


Fig. 22. Temperature Contours for all Materials of Hexagonal cross-section

Based on the results of Fig 22, the percentage relative lengths of the thermal zones along the channel for different cases are shown in Fig.23.

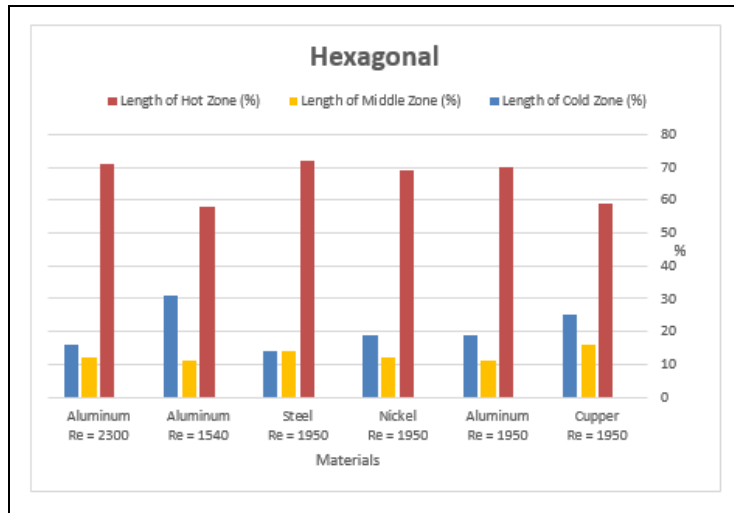


Fig. 23. Bar chart for the Hexagonal shape identifying the three zones

It is clear from Fig.23 that at the same Reynolds number of 1950, the longest cold zone has a percentage relative lengths of $L_c = 25\%$ and $L_h = 59\%$ for the copper material. When considering aluminum as the wall material at different values of Reynolds number, the longest cold zone has a percentage relative lengths of $L_c = 31\%$ and $L_h = 58\%$ at $Re = 1540$.

6.2.3 Sinusoidal cross-section

Fig. 24 shows the temperature contours along the channel as well as at entrance and exit section for $Re = 1950$ and aluminum material.

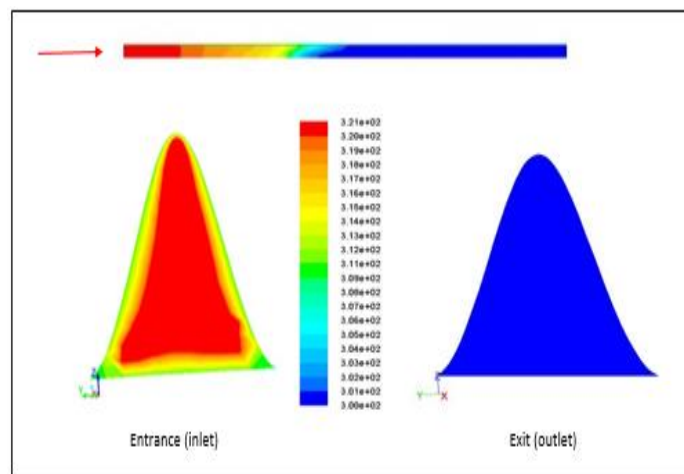


Fig. 24. Temperature Contours $Re = 1950$, Aluminum material

It is clear from Fig.24 that the temperature inside the channel drops from the inlet temperature to the wall temperature well before exiting the channel. The pattern of temperature contours at entrance and exit of the channel is repeated for all cases. However, the temperature contours along the channel length changes from one case to another depending on the case parameter.

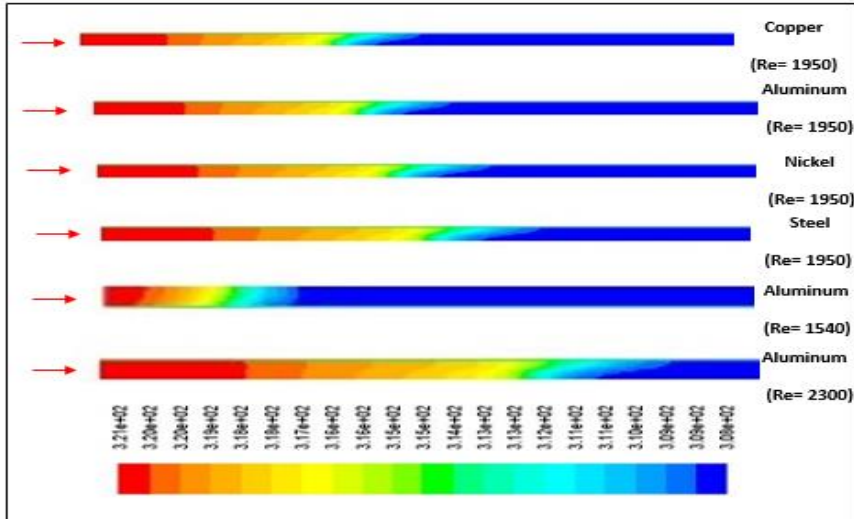


Fig. 25. Temperature Contours for all Materials of Sinusoidal cross-section

Fig.25 shows the temperature contours along the channel length for all cases. Based on the results of Fig 25, the percentage relative lengths of the thermal zones along the channel for different cases are shown in Fig.26

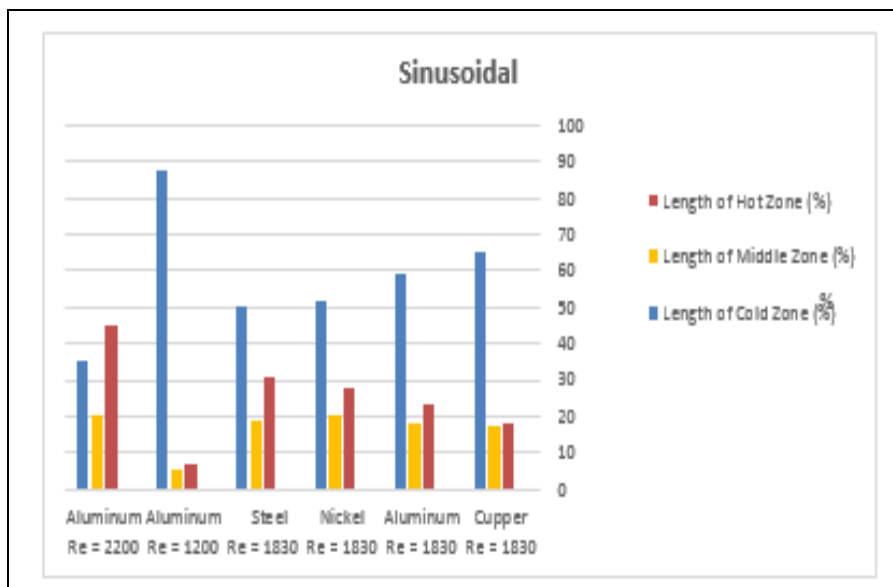


Fig. 26. Bar chart for the Sinusoidal shape identifying the three zones

Fig.26 illustrates that at the same Reynolds number of 1950, the longest cold zone has percentage relative lengths of $L_c = 65\%$ and $L_h = 18\%$ for the copper material. When considering aluminum as the wall material at different values of Reynolds number, the longest cold zone has a percentage relative lengths of $L_c = 88\%$ and $L_h = 7\%$ at $Re = 1540$.

6.2.4 Overall view of all cases

Based on the results of the previous sections an overall view of all cases can be demonstrated. Table. 2 illustrates overall results of the percentage relative lengths of all cases. Also, Fig. 27 shows the percentage relative length of cold zone (L_c) for the best cooling cases.

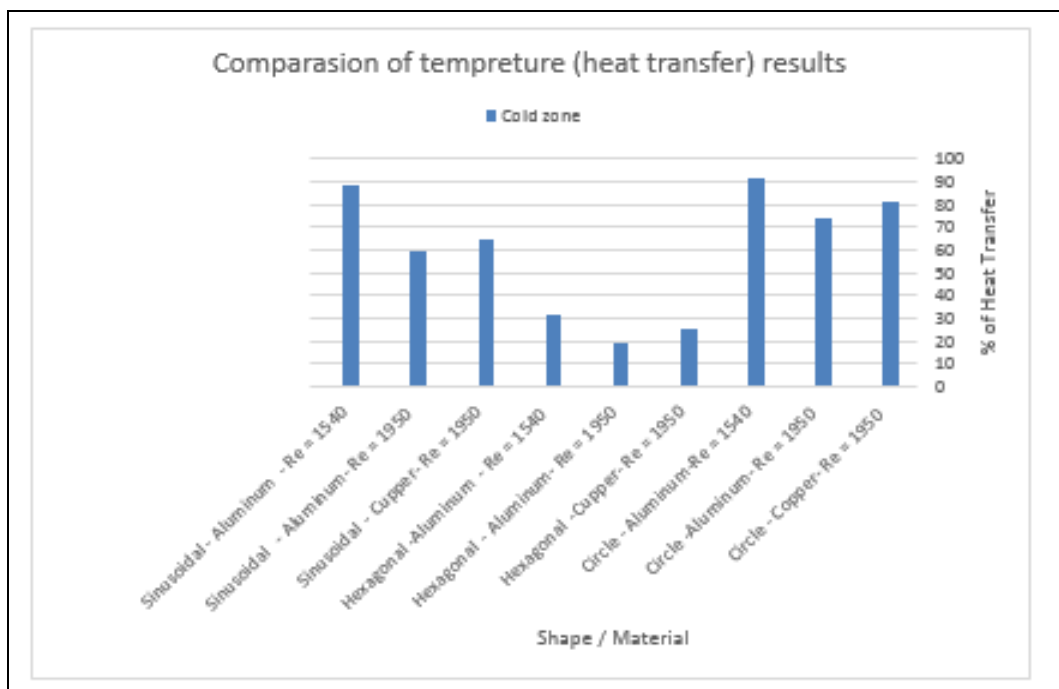


Fig. 27. Bar chart for all three shapes and Materials showing the best cooling zones

From Table.2 and Fig.27, it can be concluded that the optimum thermal cooling case can be stated as:

- When considering the same Reynolds number ($Re = 1950$) with different materials:
 1. Reynolds number = 1950
 2. Material cross section: Copper
 3. Shape cross-section: Circle
 4. $L_c = 81\%$

- When considering the same material (Aluminum) with different Reynolds number:
 1. Reynolds no. $Re = 1540$
 2. Material: aluminum
 3. Shape cross-section: Circle
 4. $L_c = 91\%$




Shape	Material	Length of Hot Zone (%)	Length of Middle Zone (%)	Length of Cold Zone (%)
Circle 	Copper $Re = 1950$	10	9	81
	Aluminum $Re = 1950$	14	12	74
	Nickel $Re = 1950$	17	15	68
	Steel $Re = 1950$	20	13	67
	Aluminum $Re = 1540$	5	4	91
	Aluminum $Re = 2300$	22	18	60
Hexagonal 	Copper $Re = 1950$	59	16	25
	Aluminum $Re = 1950$	70	11	19
	Nickel $Re = 1950$	69	12	19
	Steel $Re = 1950$	72	14	14
	Aluminum $Re = 1540$	58	11	31
	Aluminum $Re = 2300$	71	12	16
Sinusoidal 	Copper $Re = 1950$	18	17	65
	Aluminum $Re = 1950$	23	18	59
	Nickel $Re = 1950$	28	20	52
	Steel $Re = 1950$	31	19	50
	Aluminum $Re = 1540$	7	5	88
	Aluminum $Re = 2300$	45	20	35

Table 2: Study results

7. Conclusions

In the present research work, a computational study of heat conservation wheel is carried out for different materials and cross sectional shapes. Also, the Reynolds

number of flow is considered as an important parameter. The main objective of the study is to find the combination of parameters that gives the optimum performance (best heat transfer). The performance is evaluated by modeling the channel flow of the wheels. Modeling is carried out by the commercial software package ANSYS-FLUENT. Based on the discussions of section 6, the following concluding points can be stated:

4. Concerning the best thermal performance, the three investigated shapes can be arranged as: Circle, Sinusoidal and Hexagonal, respectively.
5. Although the Hexagonal section has good structural advantages, it is not the best choice when concerning the thermal performance.
6. In spite of its simplicity, the circle cross-section gives much better thermal performance than the sinusoidal cross-section that is commonly used in conservation wheels.
7. For all the best test cases, the investigated materials can be arranged according to their thermal performance from best to worst as: Copper, Aluminum, Nickel and then Steel.
8. In the range of operating values of Reynolds number (1540, 1950, 2300), the best thermal performance was recorded at the lowest value of 1540.
9. It must be pointed out that the above concluding points are based on the considered flow and thermal fields. Other concluding remarks may be obtained for other operating conditions.

8. Future Work

The following suggestions can be considered for future work as an extension of the present study:

1. The effect of the thickness of the channel wall on the thermal performance can be considered.
2. The effect of wheel rotation on both the flow and thermal fields can be included by utilizing the technique of moving grid (mesh).
3. Further investigation is needed to find out the availability of the proposed cross-sections from the structure and construction points of view
4. Expanding the study by considering the economical point of view when choosing the optimum channel material.

9. Acknowledgments

This work was supported by Umm Al-Qura University and has been performed as part of the fulfillment of the master degree. I thank my advisors who guided me through this work: Prof. Muhammad Naeem Radhwi and Prof. Ahmed Farouk Abdel Gawad.

10. References:

1. A. Pesaran, A.F. Mills, Moisture transport in silica gel packed bed I. Theoretical study, *International Journal of Heat and Mass Transfer* 30 (1987) 1037–1049.
2. A. Pesaran, A.F. Mills, Moisture transport in silica gel packed bed II. Experimental study, *International Journal of Heat and Mass Transfer* 30 (1987) 1051–1060.
3. W. Zheng, W.M. Worek, Numerical simulation of combined heat and mass transfer process in a rotary dehumidifier, *Numerical Heat Transfer Part A* 23 (1993) 211–232.
4. Y.J. Dai, R.Z. Wang, H.F. Zhang, Parameter analysis to improve rotary desiccant dehumidification using a mathematical model, *International Journal of Thermal Sciences* 40 (2001) 400–408.
5. J.L. Niu, L.Z. Zhang, Performance comparisons of desiccant of desiccant wheels for air dehumidification and enthalpy recovery, *Applied Thermal Engineering* 22 (2002) 1347–1367.
6. F. Esfandiari Nia, D.V. Paassen, M.H. Saidi, Modeling and simulation of desiccant wheel for air conditioning, *Energy and Buildings* 38 (2006) 1230–1239.
7. L.A. Sphaier, W.M. Worek, Analysis of heat and mass transfer in porous sorbents used in rotary regenerators, *International Journal of Heat and Mass Transfer* 47 (2004) 3415–3430.
8. G. Heidarinejad, H. Pasdar Shahri, S. Delfani, The effect of geometrical characteristics of desiccant wheel on its performance, *International Journal of Engineering Transactions B: Application* 22 (2009) 63–75.
9. Kodama, T. Hirayama, M. Goto, T. Hirose, R.E. Critoph, The use of psychometric charts for the optimization of a thermal swing desiccant wheel, *Applied Thermal Engineering* 21 (2001) 1657–1674.
10. H.M. Henning, T. Erpenbeck, C. Hindenberg, I.S. Santamiria, The potential of solar energy use in desiccant cooling cycles, *International Journal of Refrigeration* 24 (2001) 220–229.
11. ASHRAE, 2005 ASHRAE Handbook Fundamentals SI Edition, ASHRAE, Atlanta, (2005).
12. P. Mavroudaki, C.B. Beggs, P.A. Sleight, S.P. Halliday, The potential for solar powered single-stage desiccant cooling in southern Euro, *Applied Thermal Engineering* 22 (2002) 1129–1140.
13. S.P. Halliday, C.B. Beggs, P.A. Sleight, The use of solar desiccant cooling in the UK: a feasibility study, *Applied Thermal Engineering* 22 (2002) 1327–1338.
14. L.Z. Zhang, J.L. Niu, A pre-cooling Munters environmental control desiccant cooling in combination with chilled-ceiling panels, *Energy* 28 (2003) 275–292.

15. T.S. Ge, Y. Li, R.Z. Wang, Y.J. Dai, A review of the mathematical models for predicting rotary desiccant wheel, *Renew. Sustain. Energy Rev.* 12 (2008) 1485–1528.
16. R.B. Holmberg, Combined heat and mass transfer in regenerators with hygroscopic materials, *ASME J. Heat Transfer* 101 (1979) 205–210.
17. J.Y. San, S.C. Hsiau, Effect of axial solid heat conduction and mass diffusion in a rotary heat and mass regenerator, *Int. J. Heat Mass Transfer* 36 (8) (1993) 2051–2059.
18. D. Charoensupaya, W.M. Worek, Effect of adsorbent heat and mass transfer resistances on performance of an open cycle adiabatic desiccant cooling system, *Heat Recov. Sys. CHP* 8 (6) (1988) 537–548.
19. S.B. Riffat, A.P. Warren, R.A. Webb, Rotary heat pump driven by natural gas. *Heat Recovery Systems CHP* 15 (1995) ;(15):545–54.
20. H.J. Sauer Jr, R.H. Howell, Promise and potential of air-to-air energy recovery systems. *International Journal of Refrigeration* (1981) ;(4):182–94.
21. W. Zhuang, V.N. Roderick, Finn Borup a Department of Control Engineering, Aalborg University, Fredrik Bajers Vej 7C, Aalborg, DK-9220, Denmark b Mathematical Modelling and Computational Sciences, Wilfrid Laurier University, (1995)
22. Fluent guide manual, (2011).